Available online at www.sciencedirect.com

ScienceDirect

Advances in Space Research xxx (xxxx) xxx

ADVANCES IN SPACE RESEARCH (a COSPAR publication)

www.elsevier.com/locate/asr

Deepening of radiation belt particles in South Atlantic Anomaly Region: A scenario over past 120 years

Pankaj K. Soni *, Bharati Kakad, Amar Kakad

Indian Institute of Geomagnetism, New Panvel (West), Navi Mumbai, India

Received 8 June 2021; received in revised form 25 November 2021; accepted 29 November 2021

Abstract

The geomagnetic field has an unusual weak spot over South America and the South Atlantic Ocean, called South Atlantic Anomaly (SAA). We know that the magnetospheric particles trapped in the geomagnetic field move to the deeper altitudes over the SAA, resulting in the lower inner boundary of the radiation belt. However, over the past 400 years, the magnetic field in the SAA region has decreased consistently. In some recent studies, a rapid decrease of the magnetic field in the SAA region and the possibility of splitting of SAA have been reported. This weakened geomagnetic field has a bearing on the lower altitudinal reach (deepening) of the radiation belt particles. In this context, we performed simulations to examine and quantify the lowest altitudes encountered by the radiation belt particles over the SAA region. We found that particles of energies 100 keV-50 MeV, initially entering from an altitudes of 1–2 Earth radii are moving closer to the Earth at the rate of $3.8 - 4.7$ km/year, which results in approximately $434 - 590$ kms decrease in their altitude over the SAA region during 1900 to 2020. Furthermore, we noticed that the lowest altitude encountered by the particle in the SAA region is dependent on the initial longitude and independent of its initial local pitch angle corresponding to its entry in the Earth's magnetosphere.

© 2021 COSPAR. Published by Elsevier B.V. All rights reserved.

Keywords: Test-particle simulation; South Atlantic Anomaly; Radiation belts; Earth's inner magnetosphere

1. Introduction

The Earth possesses magnetic field that forms a magnetic field cavity around the planet termed as the magnetosphere. The magnetic field deflects highly energetic charged solar wind particles approaching the Earth, thereby acting as a protective shield for life on the Earth. Some of the charged particles are trapped in the Earth's magnetic field, and they populate different regions of the magnetosphere, such as the magnetosheath and plasmasphere, apart from the ring current and radiation belts (Ebihara and Miyoshi, 2011). The radiation belts are the regions where energetic charged particles are held by the geomagnetic field (Millan and Baker, 2012). The Earth's magnetosphere includes the inner and outer radiation belts, with the region separating the belts is called the slot region. The energetic charged particles that get trapped in this region acquire higher energies through wave-particle interactions (Mozer et al., 2013), and they have an adverse effect on the spacecraft and satellites. The observation from Van Allen Probes shows that the outer radiation belt can be split into multiple belts (Baker et al., 2013). Whereas the inner belt is relatively stable and located in the region between one to three Earth radii. It contains protons and electrons with energies of the order of hundreds of MeV and keV, respectively (Ripoll et al., 2020).

The charged particles trapped in the Earth's inner magnetosphere perform three quasi-periodic motions: gyration around magnetic field lines, bounce over magnetic mirror points, and azimuthal drift around the Earth. A set of three

* Corresponding author.
E-mail addresses: pankajs123321@gmail.com (P.K. Soni), bharati.kakad@iigm.res.in (B. Kakad), amar.kakad@iigm.res.in (A. Kakad).

https://doi.org/10.1016/j.asr.2021.11.041
0273-1177/© 2021 COSPAR. Published by Elsevier B.V. All rights reserved.

Please cite this article as: P. K. Soni, B. Kakad and A. Kakad, Deepening of radiation belt particles in South Atlantic Anomaly Region: A scenario over past 120 years, Advances in Space Research, https://doi.org/10.1016/j.asr.2021.11.041

adiabatic invariants defines their stable drift shells in which they encircle the Earth (Mukherjee and Rajaram, 1981). These bouncing-drifting magnetospheric charged particles approach close to Earth in the South Atlantic Anomaly (SAA) region, where the geomagnetic field is weak. The SAA is widely referred to as a dent in the Earth's magnetic field, and similar to the polar regions, where magnetic field lines are open, it is a favourite gateway for the energetic particles of the magnetosphere (Heirtzler, 2002). As a result, the inner radiation belt is the closest to the Earth over the SAA region (Rodrigues et al., 2019; Zhu and Liu, 2020). Over the past few centuries, the magnetic field in the SAA region has decreased consistently with the increased extent and the westward movement of the anomaly (Gillet et al., 2013). The effect of the weakening of the magnetic field in the SAA region on the lower boundary of the inner radiation belt has not been investigated so far. A question that arises is if the geomagnetic field continues to decrease at the present rate, then how much closer will, the energetic charged particles come in the SAA region. In the present study, we have examined this aspect and provide quantitative analysis.

We performed a three-dimensional test particle simulation of energetic charged particles trapped in the Earth's magnetosphere by the geomagnetic field, which was realistically modelled by utilizing coefficients of the latest generation International Geomagnetic Reference Field (IGRF) model (Alken et al., 2020). We aim to understand the sole effect of secular variation of magnetic field on the lowest altitude encountered by the radiation belt particles during its drift motion, particularly over the SAA region. This variation of the lowest altitude is referred as "deepening of particle" hereafter. We used the IGRF model to incorporate geomagnetic field in the simulation system. The change in the deepening of the inner radiation belt charged particles and its location is quantified in response to the secular variation of geomagnetic field during 1900–2020. Quantitative estimates of deepening rate of radiation belt particles will help us to understand future radiation dose enhancement in the SAA region. The paper is organized as follows. Section 2 deals with simulation model structure describing equation of motion, magnetic field configuration, and simulation inputs. Section 3 gives the simulation results of particle deepening and their variation during the year 1900–2020. Finally, the present study is discussed and concluded in Section 4 and Section 5, respectively.

2. Methodology

2.1. Model structure

We traced the motion of a relativistic charged particle with charge q and mass m in the presence of the Earth's magnetic field by considering the following governing equation of motion, Öztürk (2012):

$$\frac{d\boldsymbol{R}}{dt} = \frac{\gamma m v^2}{2qB^2}\left(1 + \frac{v_\parallel^2}{v^2}\right)\hat{\boldsymbol{b}} \times \nabla B + v_\parallel \hat{\boldsymbol{b}}, \tag{1}$$

$$\frac{dv_\parallel}{dt} = -\frac{\mu}{\gamma^2 m}\hat{\boldsymbol{b}}\nabla B. \tag{2}$$

Here, $\boldsymbol{R}$ is the position of the guiding center, γ is the relativistic factor given by $\gamma = (1 - v^2/c^2)^{-1/2}$, μ is the magnetic moment given by $\mu = \gamma^2 m v_\perp^2/2B$, $v_\parallel$ and $v_\perp$ are the parallel and perpendicular components of the velocity vector, and $\hat{b}$ is the unit vector in the direction of the local magnetic field. Eqs. (1) and (2) pertain to the guiding-center approximation, wherein the motion of a charged particle is averaged over a gyration to trace its guiding center.

The input parameters in the simulation are charge (q), mass (m), kinetic energy (E_k), local pitch angle (α_0), and initial position $[x_0 = rcos\theta cos(\phi), y_0 = rcos\theta sin\phi, z_0 = rsin\theta]$. Here, r, θ, and ϕ are the particle's distance from center of the Earth, geographic latitude, and longitude, respectively. The geographic longitude ϕ was measured positive eastward from Greenwich, and it varies from -180° to 180°. The initial velocity v_0 of a particle was estimated from its energy as follows:

$$v_0 = c\sqrt{1 - \left(\frac{m_0c^2}{m_0c^2 + E_k}\right)^2}. \tag{3}$$

Particles with energy E_k can enter the Earth's magnetosphere from any latitude and longitude. The angle between a particle's velocity vector ($\overrightarrow{v}$) and the local magnetic field ($\overrightarrow{B}$) is termed pitch angle. We placed a particle in space at the initial position $[r, \theta, \phi]$ with the velocity components $v_x = v_0 sin\alpha_0 cos\psi, v_y = v_0 sin\alpha_0 sin\psi$, and $v_z = v_0 cos\alpha_0$. Here, α_0 is the local pitch angle. We have taken initial latitude, $\theta_0 = 0^\circ$. Here, $\psi = \phi + 180^\circ$ is the gyro-phase of the particle. The gyro-phase is the angle made by the perpendicular velocity component with the positive x-direction, and it decides the particle's position in the horizontal xy- plane.

The Eqs. (1) and (2) are solved numerically using a sixth-order Runge–Kutta method as discussed in Soni et al. (2020). The expression for the sixth-order Runge–Kutta method is as follows,

$$x^{t+\triangle t} = x^t + \frac{\triangle t}{5}\left[\frac{16k_1}{27} + \frac{6656k_3}{2565} + \frac{28561k_4}{11286} - \frac{9k_5}{10} + \frac{2k_6}{11}\right]. \tag{4}$$

Here, $x^{t+\triangle t}$ is the Runge–Kutta approximation of x at time $(t + \triangle t)$, which is determined by the present value x^t plus the weighted average of six increments k_1 to k_6. The expressions of these increments are given in Luther (1968). In discretized form, Eqs. (1) and (2) give a total of four equations, which gives the rate of change of x, y, z, and $v_\parallel$ with respect to time. Similarly, we computed y, z, and $v_\parallel$. The time step in the simulation is taken as 0.01. The test-particle simulations are performed in the Cartesian coordinate system, with the positive x, y, and z directions being the upward, eastward, and northward directions. The simulation output was converted into the spherical coordinate system (r, θ, ϕ). To solve Eqs. (1) and (2), one has to provide the Earth's magnetic field configuration, which is discussed in the next subsection.

2.2. Magnetic field configuration

Mathematically, the Earth's magnetic field $\boldsymbol{B}$ can be described as the negative gradient of a scalar potential function V:

$$\boldsymbol{B} = -\nabla V. \quad (5)$$

The scalar potential function V can be represented by a series of spherical harmonics:

$$V(r, \lambda, \phi) = R_e \sum_{n=1}^{N} \left(\frac{R_e}{r}\right)^{n+1} \sum_{m=0}^{n} \left[g_n^m cos(m\phi) + h_n^m sin(m\phi)\right] P_n^m(\lambda). \quad (6)$$

Here, λ is co-latitude, $90^\circ - \theta$. As seen in Eq. (6), the Earth's magnetic field can be analytically represented by a series of spherical harmonics that include Gaussian coefficients and associated Legendre polynomials (Navabi and Barati, 2017). These spherical harmonic coefficients can be derived from long-term data obtained from ground magnetic observatories and magnetometers onboard low Earth-orbiting satellites, as in the case of the IGRF model. We used Gauss coefficients based on the IGRF model to compute the Earth's magnetic field as a latitude, longitude, and altitude function during 1900–2020. The IGRF is a well-established model (Thébault et al., 2015) widely used to understand the secular variation of the Earth's intrinsic magnetic field generated by the process of geodynamo (Liu and Olson, 2009; Suttie et al., 2011). We obtained the set of Gaussian coefficients g_n^m and h_n^m from the IGRF model https://www.ngdc.noaa.gov/IAGA/vmod/igrf.html. The International Association of Geomagnetism and Aeronomy, a working group, examines high-quality and globally distributed geomagnetic field observations and updates the coefficients every five years. $P_n^m(\lambda)$ represents the Schmidt quasi-normalized associated Legendre functions of degree n and order m. We have implemented these mathematical steps in the computation by following (Navabi and Barati, 2017). The scalar potential defined in Eq. (6) was used together with Eq. (5) to obtain the magnetic field components $[B_r, B_\theta, B_\phi]$ at a given location.

Figs. 1(a) and 1(b) show maps of the total intensity of the surface geomagnetic field for the years 1900 and 2020, respectively. The most prominent anomalous feature is the low magnetic field over the South Atlantic Anomaly region, as apparent in blue color. Fig. 1 indicates that the magnetic field in the SAA region has decreased from 1900 to 2020 and that the region's area increased significantly. Researchers have actively studied the consistent decrease in the Earth's magnetic field in the SAA region (Finlay et al., 2016b; Campuzano et al., 2019). The effect of this decreasing geomagnetic field in the SAA region on the deepening of the inner radiation belt charged particles is analyzed by solving Eqs. (1), and (2) in the presence of a realistic magnetic field. The results are discussed in the next section.

3. Results

3.1. Variation of altitude of charged particles during drift-bounce motion

We carried out a three-dimensional test-particle simulation to analyze the effect of spatio-temporal variations in the geomagnetic field on the lowest altitude encountered by the inner radiation belt particle during their drift motion around the Earth. In simulation model, the geomagnetic field is incorporated using IGRF model and the particle trajectories are simulated by solving equation of motion. We obtained Gaussian coefficients for 1900 to 2020 at the interval of 10-years and tracked the proton's trajectory. The proton of particular energy is initiated from a fixed location $[H_0 = r_0 - R_e, \theta_0, \phi_0]$, and their trajectories are obtained from simulation. We chose different values of energy in the range of 10 keV to 50 MeV and two values of altitudes (i.e., $H_0 = 1R_e$ and $H_0 = 2R_e$, here $R_e = 6371km$) at time $t = 0$. The proton was introduced at the geographic equator ($\theta_0 = 0^\circ$) outside the anomaly region at a fixed longitude, and the simulation was carried out for one azimuthal drift around the Earth.

As an example, the simulated trajectory of the 10 MeV proton initially placed at $[H_0 = 1R_e, \theta_0 = 0^\circ, \phi_0 = 120^\circ]$ is shown in Fig. 2 for the year 2020. The trajectory was obtained under the guiding-center approximation, implying that the proton's gyro-motion around the magnetic field line was averaged over a gyration to trace the guiding center of the particle. Fig. 2(a) shows the proton bouncing along magnetic field lines and drifting around the Earth. The color bar represents the magnetic field strength at the Earth's surface, and the SAA region is apparent in blue color. The tilt of the magnetic field axis with respect to the Earth's geographic axis, along with the low magnetic field in the SAA region, result in the latitudinal asymmetry in the proton motion in the northern and southern hemisphere. We noticed that as the bouncing-drifting proton approaches the SAA region, it starts to come closer to the Earth and attains lower altitudes. It is because the proton encounters gradients in the magnetic field not only in radial direction but also in azimuthal direction (i.e., ∇B_ϕ) while moving across the SAA region. Therefore, the protons drifting around the Earth in the near-equatorial region ($\sim -15^\circ < \theta < 15^\circ$) are pushed earthward in the SAA region through $\overrightarrow{B} \times \nabla B_\phi$ drift (Chen et al., 1984). The proton's trajectory projected on the xy– plane in geographical coordinates, as seen from the south geographic pole, is shown in Fig. 2(b). Here, the Earth is represented by a

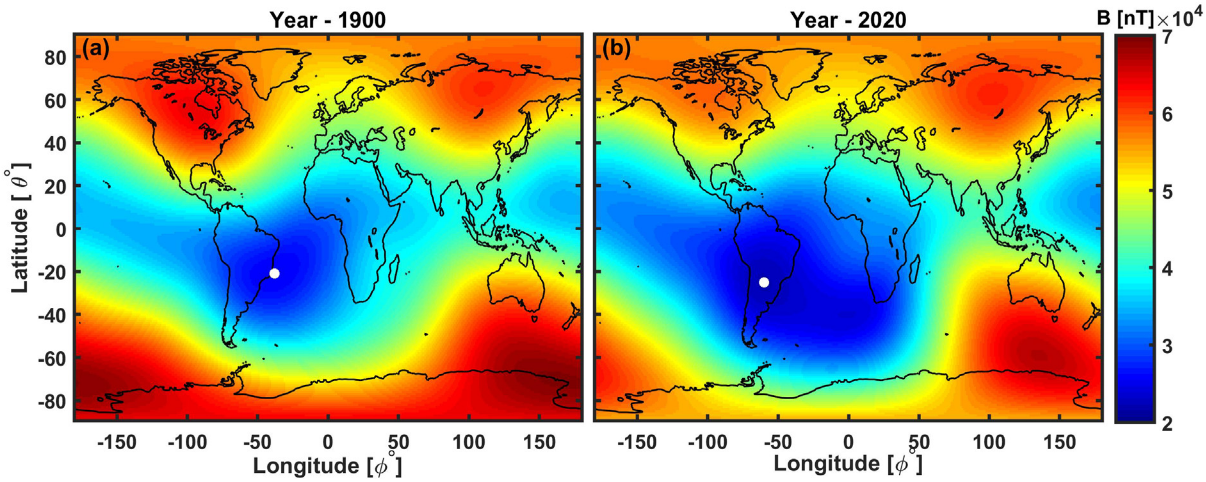

Fig. 1. Variation of the Earth's surface magnetic field for the years (a) 1900 and (b) 2020 estimated from the IGRF model. The white dots represent surface locations with the lowest magnetic field strength in the SAA region.

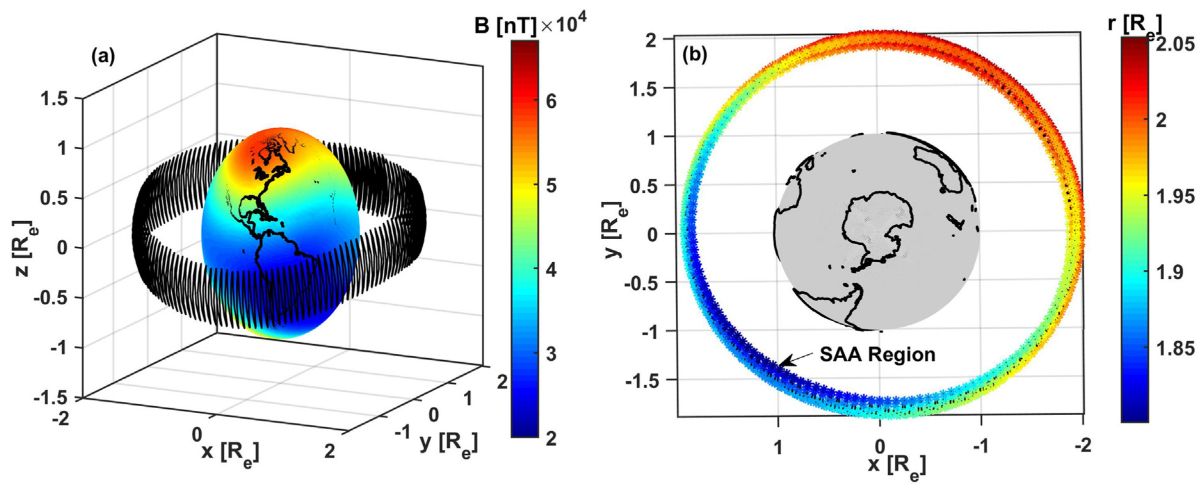

Fig. 2. The trajectory of a 10 MeV proton with a pitch angle of 89° initiated from $[H_0 = 1R_e, \theta_0 = 0^\circ, \phi_0 = 120^\circ]$ in the Earth's magnetic field for 150 s. (a) The color bar represents the magnetic field intensity, and the proton trajectory is shown by the black ring. (b) A top view of the proton's motion as seen from the south geomagnetic pole. The color bar represents the proton's radial distance, r from the Earth's center.

sphere centered at the origin. The color bar represents the radial distance r of the proton from the center of the Earth in units of Earth radii. The trajectory shown in Fig. 2 reveals that a bounce-drifting proton introduced at $[H_0 = 1R_e, \theta_0 = 0^\circ, \phi_0 = 120^\circ]$ approaches closer to the Earth in the longitudinal zone of 130°W to 20°E, which corresponds to the SAA region. This longitudinal zone is marked by an arrow in Fig. 2(b).

First, we explain the method to find the minimum altitude of the particle in the SAA region. The minimum altitude encountered by particle during its drift motion is the altitude corresponding to the lowest magnetic field (B_{min}) along the magnetic field line while bouncing. For one drift period ($\phi = -180^\circ$ to 180°), we simulate the particle trajectory and obtain altitude, latitude, and longitude of particle at each time step. Fig. 3(a) shows the variation of H as a function of ϕ (black dots) for one complete drift of a 10 MeV proton and its projection on the Earth with magnetic field at $1R_e$ as background, is depicted in Fig. 3(c). It is noted that for a given longitude the variation of altitude is bounded by upper and lower limits. To obtain this upper and lower boundaries, the complete particle trajectory of proton is divided in the longitudinal bin of 4°. Then, we picked the maximum and minimum altitude of the particle in each bin and noted their latitude and longitude. The maximum and minimum altitude of particle provides the upper and lower boundaries of the altitude variation experienced by the particle during its bounce-drift motion around the Earth. These altitudes are respectively denoted by H^u ("u" refers to upper) and H^l ("l" refers to lower) and marked by magenta and red dots in Fig. 3(a). We noticed that the maximum altitude corresponds to the minimum magnetic field over its bounce motion along the magnetic field line. Whereas the minimum altitude corresponds to

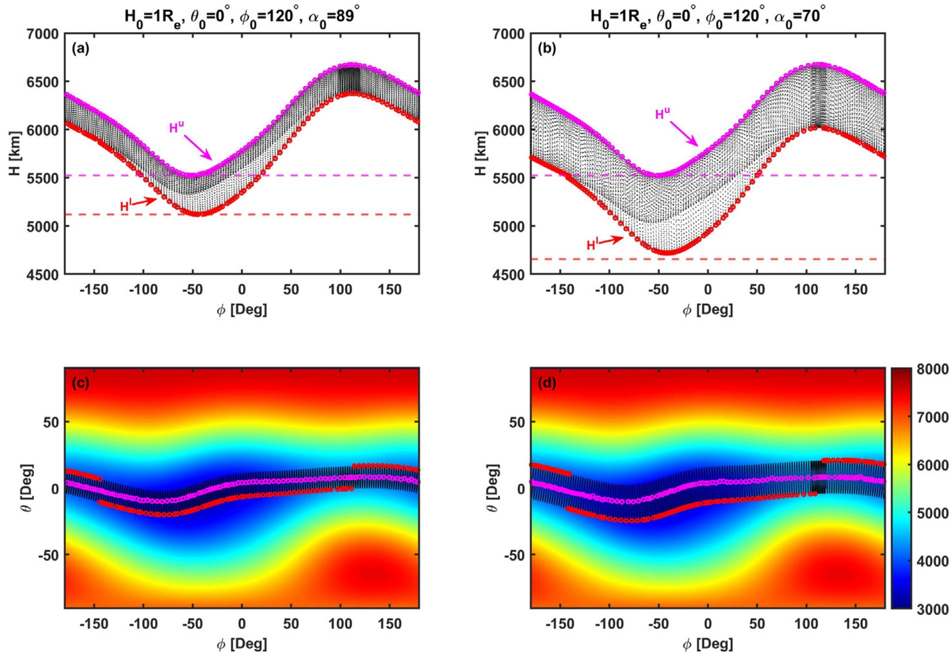

Fig. 3. Variation of altitude (H) as a function of longitude for a proton of energy 10 MeV initiated at $H_0 = 1R_e, \theta_0 = 0^\circ, \phi_0 = 120^\circ$ with $\alpha_0 = 89^\circ$ (a), and $\alpha_0 = 70^\circ$ (b). Black dots show the complete particle trajectory while magenta and red dots are corresponding to the altitude of the particle at B_{min} (say H^u) and at mirror points (say H^l) along the magnetic field line. The particle trajectory with altitudes H^u, and H_l, are projected on the Earth's magnetic field in (c) and (d). Here, Earth's magnetic field at $H_0 = 1R_e$ is shown by the colour bar. The horizontal magenta and red dashed lines in (a) and (b) are corresponding to the minimum of H^u (say H^u_{min}), and H^l (say H^l_{min}). The comparison of magenta and red lines in (a) and (b) indicates that H^u_{min} is independent of the initial pitch angle.

the maximum magnetic field experienced by the particles during their bounce motion along the field line (i.e., the location of the mirror points). For visualization, one can refer to Fig. 3(c). It may be noticed that H^u is corresponding to the B_{min}, and H^l is corresponding to one of the mirror points. The minimum value of H^u falls in the SAA region (say, H^u_{min} or deepening), and it represents the lowest altitude reached by the particle during its drift motion around the Earth. By tracing H^u, we exclude the bounce motion contributions to the altitude variation of particles. The value of H^u_{min} is marked with the horizontal magenta dashed line in 3(a), and it is used in the further analysis to examine the variation of particle's minimum altitude in the SAA region over 1900–2020.

Before we proceed it is important to verify the effect of initial pitch angle of particle on the H^u_{min}. For this purpose, we compared altitudinal variation of 10 MeV proton having local pitch angle, $\alpha_0 = 89^\circ$, and $\alpha_0 = 70^\circ$. Generally, the particles entering the Earth's magnetosphere in the near-equatorial region have peak close to 90° in pitch angle distribution Chen et al. (1999) that justifies the choice of equatorial pitch angles considered here. In Fig. 3, we have shown the variation of altitude as a function of longitude for a proton of energy 10 MeV initiated at $[H_0 = 1R_e, \theta_0 = 0^\circ, \phi_0 = 120^\circ]$ with local pitch angle of (a) $\alpha_0 = 89^\circ$, and (b) $\alpha_0 = 70^\circ$, respectively. Their corresponding trajectories are projected on the Earth with magnetic field at $1R_e$ as background and it is depicted in panel Fig. 3(c) and (d), respectively. The comparison of H^l_{min} (horizontal red dashed line) in panel (a) and (b) indicates that as the initial pitch angle of particle decreases, the altitude corresponding to mirror point decreases. It is because as the initial pitch angle of the particle decreases, the particle bounces back from higher latitudes. Our interest is in the variation in H^u, the altitude of particle corresponding to the B_{min} along the field line during its bounce motion. It is noted that H^u_{min} is less significantly affected by choice of initial pitch angle. Therefore, for further analysis, we took $\alpha_0 = 89^\circ$ while simulating trajectories of energetic particles around the Earth.

In this simulation, initial longitude (ϕ_0) is one of the input parameters, which decides the location of entry of particle in the Earth's magnetosphere. In order to examine the dependence of H^u_{min} on the initial longitude, Fig. 4 shows the variation of altitude of particle as a function of the longitude for the protons of energy 10 MeV initiated at $H_0 = 1R_e, \theta_0 = 0^\circ, \alpha_0 = 89^\circ$ with initial longitude of (a) $\phi_0 = -120^\circ$ (b)$\phi_0 = 50^\circ$ (c) $\phi_0 = 120^\circ$ for year 2020. In panels a-c, the vertical and horizontal cyan dashed lines represent the particle's initial longitude and initial altitude at $t = 0$. The decrease in the particle's altitude with respect to its initial altitude, i.e., $\delta = H_0 - H^u_{min}$ is largest over the SAA region, which is shown by the black arrow in panels (a)-(c). However, δ of the particle over the SAA varies with the value of initial longitude. To understand this tendency, the deviation δ, as a function of ϕ_0 is shown in 4(d) for ini-

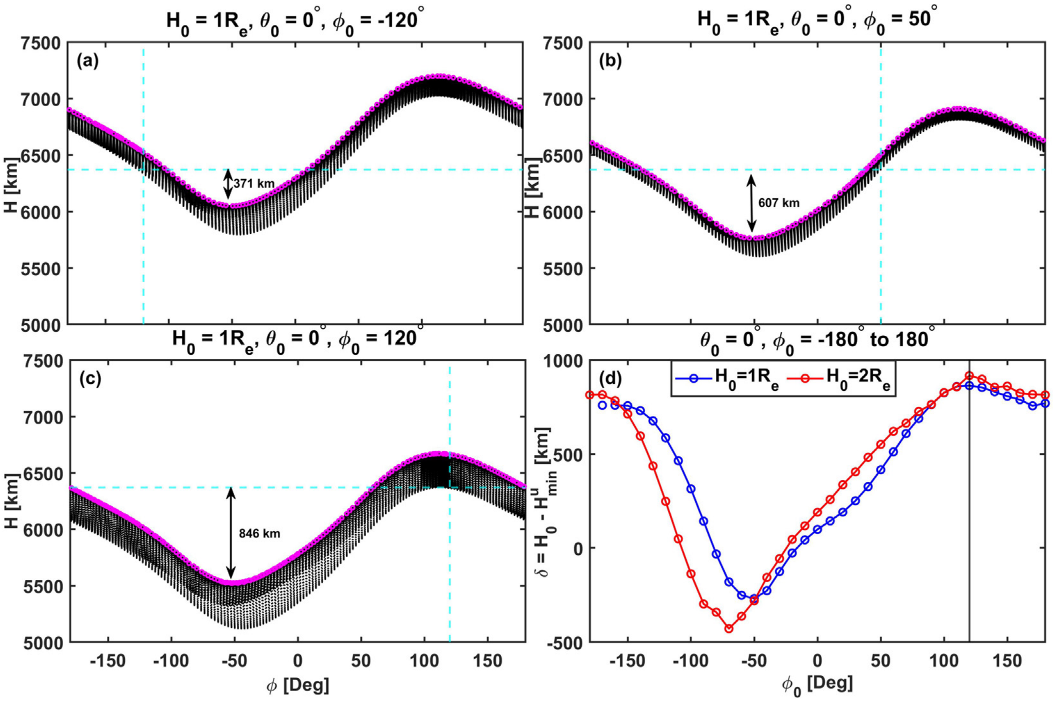

Fig. 4. Variation of altitude (H) as a function of geographic longitude for the proton of energy 10 MeV initiated at $H_0 = 1R_e, \theta_0 = 0^\circ, \alpha_0 = 89^\circ$ with initial longitude (a) $\phi_0 = -120^\circ$, (b) $\phi_0 = 50^\circ$, and (c) $\phi_0 = 120^\circ$. The initial location of the particle is marked with cyan dashed lines in each panel. The black dots in each panel show the complete particle trajectory, while magenta dots correspond to the H^u. The deepening of the particle from its initial altitude, $\delta = H_0 - H^u_{min}$ is shown by the black arrow. The deviation δ, as a function of initial longitude is shown in panel (d).

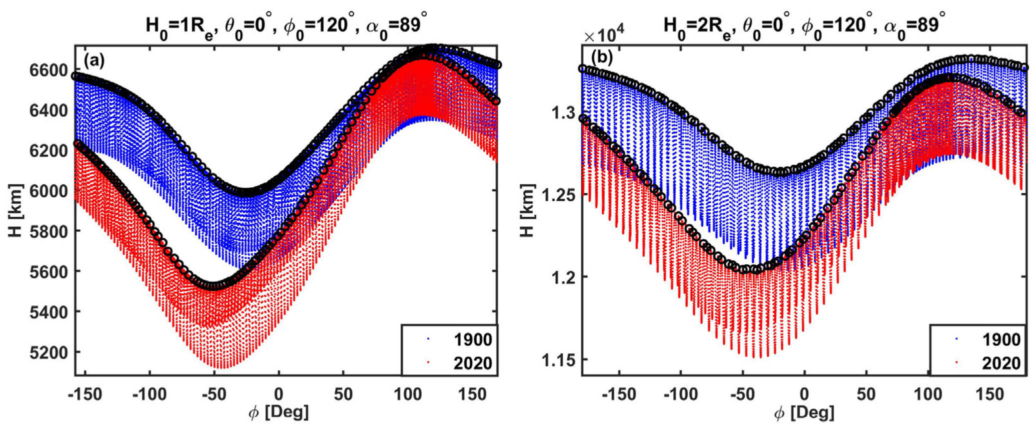

Fig. 5. Variation of the 10 MeV proton's altitude $H = r - R_e$ above the Earth's surface as a function of the geographic longitude for the years 2020 (red) and 1900 (blue) for different initial locations: (a) $H_0 = 1R_e$ and (b) $H_0 = 2R_e$. The black circles provide the upper boundary (H^u) of altitude variation and it represents the altitude of the proton associated with B_{min} experienced by particle during their bounce motion.

tial altitude of $H_0 = 1R_e$ (blue), and $H_0 = 2R_e$ (red). It is found that δ is largest when the particle is initiated close to $\phi_0 = 120^\circ$ (shown by vertical black line). Therefore, we have used initial longitude $\phi_0 = 120^\circ$ for the further analysis. The physical reason for this dependence is discussed later in Section 4.

Next, variation of the proton's altitude (H) as a function of the longitude is shown in Fig. 5 for the years 2020 (red) and 1900 (blue). Figs. 5(a) and 5(b) show the variation for cases when the proton was initially placed at $H_0 = 1R_e$ and $H_0 = 2R_e$, respectively. This altitude corresponding to the minimum magnetic field (B_{min}) along the proton's bounce motion (i.e., H^u) is marked with the black circles in each panel. The altitude variation shows an inverted-bell shape, with the lowest altitude being in the SAA region owing to the lower magnetic field strength. The spread in the proton's altitude at a fixed longitude for both years (depicted by red and blue dots) is attributed to the bounce motion of the proton. Evidently, for both altitudes, the longitude corresponding to the minimum altitude H^u_{min} of the proton shows a westward shift in 2020 as compared to that of the year 1900. The westward shift apparent in H^u_{min} is caused by

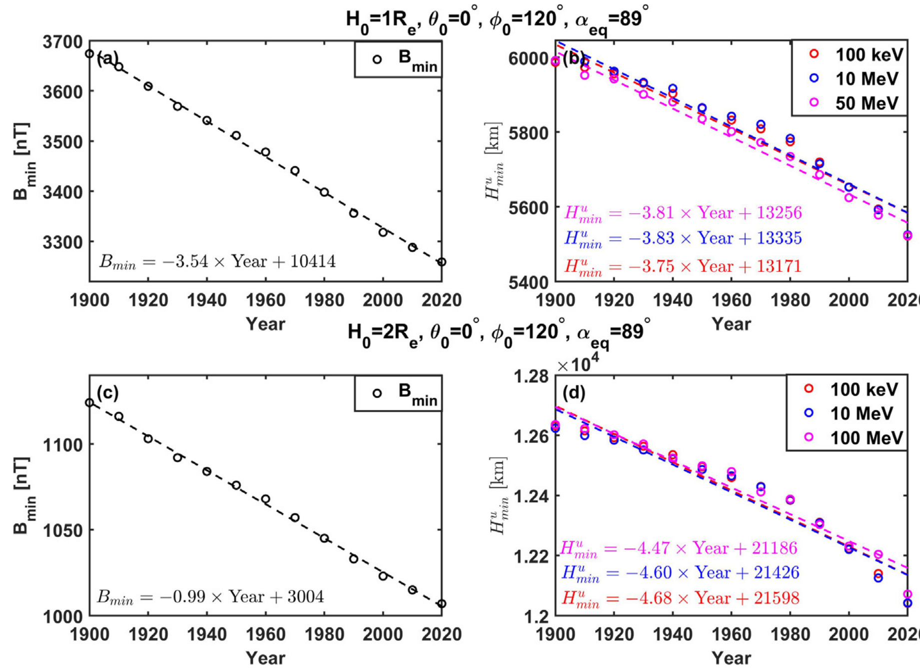

Fig. 6. Time variation of the minimum magnetic field intensity (B_{min}) over the globe is shown at (a) $H_0 = 1R_e$, and (c) $H_0 = 2R_e$. The time variation of the minimum altitude reached by proton of energy 100 keV (red), 10 MeV (blue), and 50 MeV (magenta) initially placed at (b) $H_0 = 1R_e$, and (d) $H_0 = 2R_e$, respectively in the SAA region.

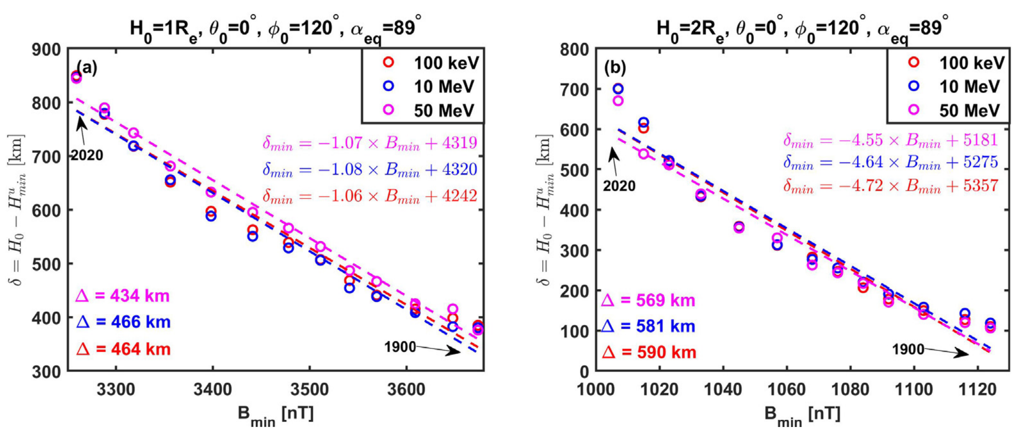

Fig. 7. The variation of depth, $\delta = H_0 - H^u_{min}$ of protons initially placed at (a) $H_0 = 1R_e$ and (b) $H_0 = 2R_e$ with energy 100 keV (red), 10 MeV (blue), and 50 MeV (magenta) as a function of minimum geomagnetic field B_{min} at respective altitudes. The linear trends are fitted with least square (LS) and equations are mentioned in respective subplots.

the westward movement of the SAA region over the past decades. Furthermore, protons reached much lower altitudes in 2020 as compared to 1900. It directly implies the increase in deepening of the inner radiation belt particles over the SAA region in 2020 as compared to 1900.

We performed different simulations runs to examine the variation of H^u by considering the geomagnetic field variation from 1900 to 2020 at 10-year intervals and estimated the value of H^u_{min}. Simultaneously, we noted the minimum magnetic field intensity B_{min} over the globe at an altitude of H_0 for respective years. Fig. 6(a) and (c) shows the variation of B_{min} with time at $H_0 = 1R_e$ and $H_0 = 2R_e$, respectively. The decrease of B_{min} at the rate of 4nT/year and 1 nT/year at altitudes of $1R_e$ and $2R_e$ is evident. Fig. 6(b) and (d) shows the time variation of H^u_{min} for protons of energy 100 keV (red), 10 MeV (blue), and 50 MeV (magenta) for $H_0 = 1R_e$ and $H_0 = 2R_e$, respectively. Notably, both B_{min} and H^u_{min} are decreasing linearly with time from 1900 to 2020. Fig. 6 indicate that the steady and consistent decrease in the geomagnetic field over the past few decades has a bearing on the lower altitudes encountered by particles over SAA region while drifting around the Earth. We applied a least-squares fit to the data plotted in Fig. 6, and their regression equations are given in each subplot. These equations indicate that the minimum altitude reached by the energetic proton (100 keV - 50 MeV) in the SAA region decreases at the rate of 3.8–4.7±0.1 km/year.

Next, we obtained the empirical relation between δ and B_{min} to understand the effect of decreasing magnetic field on the deepening of the radiation belt particles. Fig. 7(a) and (b) shows the δ as a function of B_{min} for protons of energy 100 keV (red), 10 MeV (blue), and 50 MeV (magenta) for (a) $H_0 = 1R_e$ and (b) $H_0 = 2R_e$ over the period of 1900–2020. The black arrows indicate the years 1900 and 2020. This linear variation is fitted with the least square method, shown with dashed lines of respective colors. The corresponding least-square fit equations are given in each subplot in Fig. 7. The variation of δ with B_{min} has different slopes for the different altitudes. This is because the magnetic field intensity varies with the altitude. It is found that the $\Delta = (\delta_{2020} - \delta_{1900})$ has increased almost by $434 - 466$, and $569 - 590$ km in year 2020 as compare to 1900 for $H_0 = 1R_e$ and $2R_e$, respectively. It means the proton entering the Earth's inner magnetosphere at an altitude of 1–2R_e comes $434 - 590$ km closer to the Earth in 2020 compared to 1900 over the SAA region.

3.2. Location of highest deepening and its westward movement

The SAA region is also slowly changing its position due to the secular evolution of the geomagnetic field. (Heynderickx, 1996) suggested three ways to get the location of the SAA defined as the (i) mirror point of the geographic location of the center of the eccentric dipole approximation to the geomagnetic field, (ii) locus of the local minimum of the geomagnetic field at a fixed altitude and (iii) locus of the local particle flux maximum in the SAA region. Irrespective of the way used to get the SAA location, the SAA region's westward movement is observationally established, and it has been discussed in earlier studies (Pavon-Carrasco and De Santis, 2016; Ye et al., 2017). When a bounce-drifting particle approaches the SAA region (where magnetic field intensity is low), it comes close to the Earth to conserve the adiabatic invariants. However, due to the non-uniformity of the magnetic field and particle's bounce motion, the longitude corresponding to the H^u_{min} may not be the same as the location of the minimum magnetic field in SAA. In this context, we have used the simulated trajectories of charged particles and the geomagnetic field modelled by IGRF to estimate the center of the SAA during 1900–2020 at the interval of 10 years.

For this purpose, we obtained the minimum magnetic field location over the globe at a given altitude using IGRF. Next, we noted the longitude corresponding to the minimum altitude (H^u_{min}) of a particle in the SAA region using simulation, which is termed as ϕ_{min}. Fig. 8 show the trajectory of a 10 MeV proton with a initial pitch angle of 89° initially placed at $H_0 = 1R_e$ (a, c), and $H_0 = 2R_e$ (b, d). The trajectories are shown for 1900 (a, b) and 2020 (c, d). The color bar represents the magnetic field intensity at the respective altitude. The white color shows the pro-

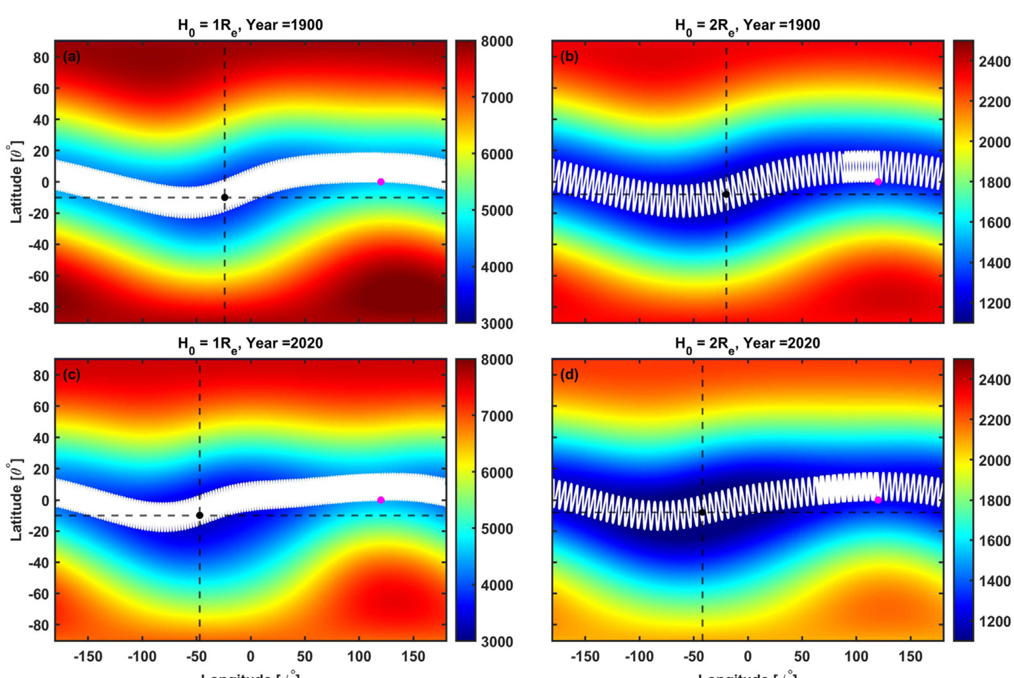

Fig. 8. The trajectory of 10 MeV proton with initial local pitch angle of 89° at an altitude of (a)-(c) $H_0 = 1R_e$, (b)-(d) $H_0 = 2R_e$ are shown for year 1900 and 2020. The color bar represents the magnetic field intensity at that altitude, and the gray color shows projection of the proton's bounce-drift trajectory on the Earth. Each panel's magenta and white dot indicate the particle's initial location and center of the SAA. The comparison of a center of SAA for 1900 and 2020 manifest the westward drift of the anomaly.

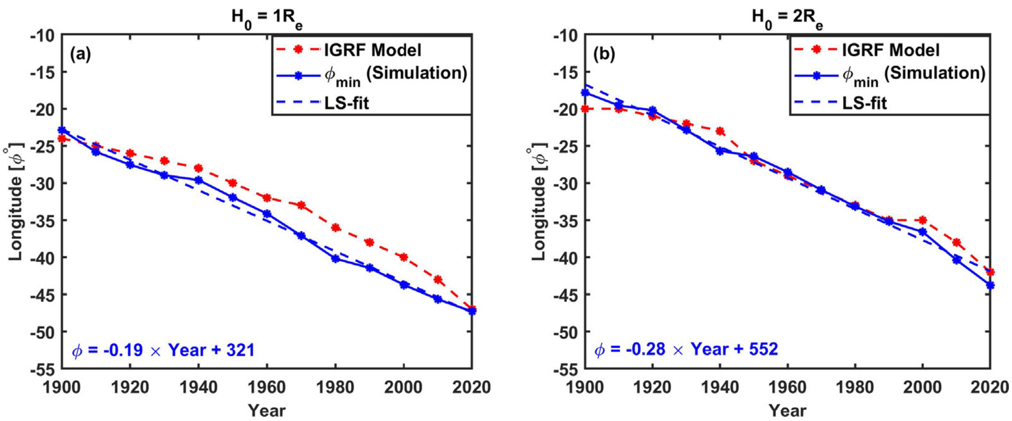

Fig. 9. The time variation of longitude corresponding to the B_{min} at (a) $H_0 = 1R_e$, and (b) $H_0 = 2R_e$ obtained from IGRF model is plotted in red color. The time variation of longitude corresponding to H^u_{min} or deepening estimated from the simulation is plotted in blue color. The least-square (LS) fit to this trend is shown by dashed lines.

ton's bounce-drift trajectory with the initial location marked by a magenta dot. The black dot in each panel indicates the center of the SAA estimated from the minimum magnetic field at that altitude. The vertical dashed lines mark the SAA's centre, reflecting the westward drift of the SAA from the years 1900 to 2020. In Fig. 9 the variation of the longitude associated with the minimum magnetic field obtained from the IGRF model (red) and the longitude corresponding to H^u_{min} (blue) are plotted from 1900 to 2020. We can see that the center of anomaly obtained from particle trajectory and the model agree well. The least-square fit of H^u_{min} conclude that the center of the anomaly is moving westward at the rate of 0.19°/year at an altitude of $1R_e$ and 0.28°/year at an altitude of $2R_e$.

4. Discussion

We have performed a three-dimensional test-particle simulation to investigate the dynamics of inner radiation belt particles in the SAA region and their variation in the last 120 years. In order to investigate this, the Earth's magnetic field is modelled by utilizing coefficients of the latest generation IGRF model that deals only with the Earth's internal field and is valid up to almost five Earth radii. Beyond this point, the magnetic field due to solar wind can no longer be neglected. Moreover, as we move away from the Earth, the contribution of dipolar and other higher-order magnetic field sources decrease rapidly. Therefore, the influence of SAA will be more pronounced at the inner radiation belt (1.1–3 R_e), and we have focused on this region. Furthermore, as higher energetic protons dominate the inner radiation belt, the chosen species for this study is a proton with energy range of 100 keV to 50 MeV, which is the observed energy range in this region (Ripoll et al., 2020).

In the simulation model, the equation of motion (guiding center approximated) is solved using the sixth-order Runge–Kutta method to achieve the numerically stable results. As the input of the simulation model, we have initiated protons of different energies at two initial altitudes (i.e., $H_0 = 1R_e$ or $2R_e$) at the geographic equator with different longitude and initial equatorial pitch angle. We noticed that the H^u_{min} is less significantly affected by the choice of initial equatorial pitch angle. As the initial pitch angle decreases, the particle bounce back from the higher altitude (corresponding to B_{max} along the field line), keeping the location of B_{min} unaffected. Furthermore, we found that in the SAA region, particles come more closer to the Earth when they enter the Earth's magnetosphere from the longitudes located outside the SAA (i.e., $\phi_0 = 120^\circ$). To understand this tendency, we estimated the gradient force, $F^{\nabla B}_{total} = \mp\frac{1}{2}qv_\perp r_L \nabla B$ (Chen et al., 1984) at each time step when the particle is drifting around the Earth. Here, $v_\perp, r_L$ are particle's perpendicular velocity and gyroradius, respectively. In Fig. 10, we have shown the variation of gradient force, $F^{\nabla B}_{total}$ along with their components in the Cartesian coordinate system as a function of longitude for (i) $\phi_0 = 50^\circ$ (blue), and (ii) $\phi_0 = 120^\circ$ (red) for a proton of energy 10 MeV initiated at [$H_0 = 1R_e, \theta_0 = 0^\circ$]. It is noticed that, magnitude of gradient force is large when proton is initiated from $\phi_0 = 120^\circ$. Thus, the longitudinal dependence evident in the simulation is attributed to the force acting on the particle due to gradient in the magnetic field.

The detail investigation of variation of H^u_{min} along with its latitude and longitude during year 1900 to 2020 for the protons of energies 100 keV, 10 MeV, and 50 MeV indicate that the minimum altitude reached by the energetic proton in the SAA region is decreasing at the rate of 3.8–4.7±0.1 km/year. It causes inner radiation belt energetic protons to reach approximately 434 – 590 km closer to the Earth in 2020 as compared to 1900. We also noticed that longitude corresponding to the H^u_{min} moves westward from the year 1900 to 2020 and the rate of westward movement is found to be 0.19°/year at an altitude of $1R_e$ and

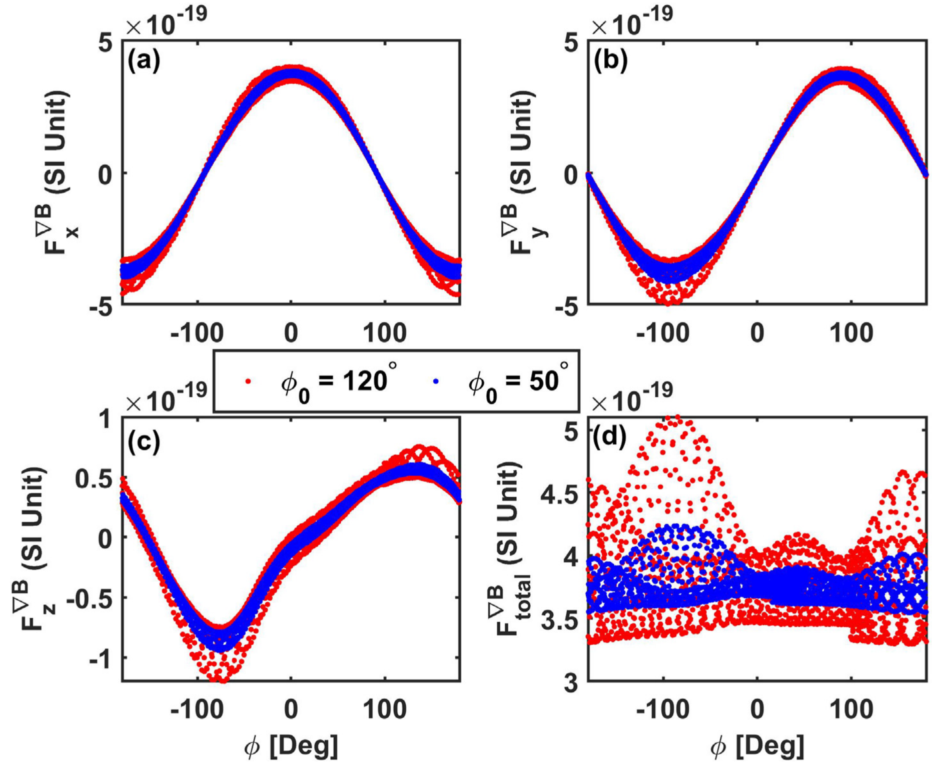

Fig. 10. Variation of gradient force along with their components as a function of longitude for initial longitude $\phi_0 = 50^\circ$ (blue), and $\phi_0 = 120^\circ$ (red) for a proton of energy 10 MeV initiated at $H_0 = 1R_e, \theta_0 = 0^\circ$.

0.28°/year at an altitude of $2R_e$. It is expected as the SAA itself is drifting westward (Gillet et al., 2013).

It may be noted that we have performed simulations using a single particle. To obtain the particle flux in the SAA region, one has to perform the simulation by taking a large number of charged particles for one complete azimuthal drift. However, such simulations are computationally very expensive. We have seen that particle's energy is less significantly affecting the deepening due to in built guiding center approximation. The protons of different energies (100 keV to 50 MeV) came 434 – 590 km closer to the Earth in 2020 as compared to 1900. It suggests that results obtained from the single-particle simulation can be applied to a large number of particles.

In addition, the particle dynamics in the SAA region are influenced by the solar flux level and the geomagnetic activity (Qin et al., 2014) as well. One requires long-term satellite observations of particle fluxes in this region with good altitudinal coverage to investigate the deepening of the energetic particles. The availability of the satellite observations for a limited period makes it difficult to quantify the effect of the weakening of the magnetic field on the deepening of energetic protons. Moreover, the particle flux observations will have a combined effect of solar flux, geomagnetic activity, and the geomagnetic field's secular variation. In particle flux, separating the sole effect of the geomagnetic field's secular variation will be challenging. In such a scenario, test-particle simulations can help understand and visualize the effect of the decreasing geomagnetic field on the radiation belt's inner boundary in the SAA region.

5. Summary and conclusions

An increase in radiation doses in the SAA region is a matter of great concern as they reflect the deepening of energetic particles to the lower altitudes. It has been predicted that the steady decrease in the Earth's magnetic field will continue in the near future with a westward drift of its center and that the magnetic moment of the Earth will decrease further (Finlay et al., 2016a). Ground and satellite observations show that the rate of decrease in the magnetic field in the SAA region has increased significantly in the last fifty years and that there is a possibility of the anomaly splitting into two regions. Also, in recent studies, it is suggested that the Earth's magnetic field can change ten times faster than previously thought (Davies and Constable, 2020). These observations underscore the potential seriousness of the increasing deepening levels of energetic particles in the SAA region.

In general, we are aware that the geomagnetic field is decreasing consistently in the SAA region. As a result, the charged particles trapped in inner radiation belts are likely to reach lower altitudes. Here, we have quantified the effect of decreasing geomagnetic fields on the energetic charged particles' deepening. For this purpose, the complete trajectory of the charged particles of different energies and altitudes are examined through test-particle simulations. Our simulation results indicate that the decrease in the SAA region's geomagnetic field is causing energetic particles of the inner radiation belts to move steadily closer to the Earth. In the last 120 years (1900–2020), the radiation belt's lower boundary has moved approximately 434 – 590 km toward the Earth. In such a scenario, the empirical relations presented in Fig. 7 are beneficial in understanding and forecasting the deepening of the radiation belt particles with the knowledge of the minimum magnetic field in the SAA region. We noticed that protons' deepening are mainly controlled by the magnetic field gradients in the SAA region. It is less significantly affected by the particle's energy. Thus, the results presented for a single particle are, in general, valid for a large number of charged particles having energies in the range of 100 keV-50 MeV. The quantitative estimates of the energetic charged particles' deepening provided here can help us analyze future enhancement of radiation dose in the SAA region.

However, the Earth's magnetic field has a more complex configuration, strongly controlled by solar wind conditions. The Earth's magnetosphere is compressed on the dayside and stretched at the night side with open field lines in the polar region. Nevertheless, the Earth's magnetic field can be approximated by the dipolar closed magnetic field line configuration in the inner magnetosphere (Baumjohann and Treumann, 2012). As we aim to examine the effect of the secular variation of the geomagnetic field on the deepening of the inner radiation belt particles, the assumption of the dipolar geomagnetic field is applicable, and the IGRF reasonably models it. The modelling of the deepening of charged particles in the presence of a more complex magnetic field configuration will be taken up as a future study to address the combined effect of geomagnetic conditions and secular variation of the magnetic field. For this purpose, realistic models like the Tsyganenko magnetic field model (Girgis et al., 2020) can be used.

Declaration of Competing Interest

The authors declare that they have no known competing financial interests or personal relationships that could have appeared to influence the work reported in this paper.

Acknowledgments

We thank NGDC NOAA for the IGRF model. The data required for the simulation model is obtained from the 13th generation International Geomagnetic Reference Field model available from https://www.ngdc.noaa.gov/IAGA/vmod/igrf.html. The model computations were partly performed on the High-Performance Computing System at the Indian Institute of Geomagnetism.

References

Alken, P., Thebault, E., Beggan, C., Aubert, J., Baerenzung, J., Brown, W. J., Califf, S., Chulliat, A., Cox, G., Finlay, C.C., et al., 2020. Evaluation of candidate models for the 13th generation international geomagnetic reference field. Version-2 available at Research Square. https://doi.org/10.21203/rs.3.rs-41022/v2.

Baker, D., Kanekal, S., Hoxie, V., Henderson, M., Li, X., Spence, H.E., Elkington, S., Friedel, R., Goldstein, J., Hudson, M., et al., 2013. A long-lived relativistic electron storage ring embedded in earth's outer van allen belt. Science 340, 186–190.

Baumjohann, W., Treumann, R., 2012. Basic Space Plasma Physics. https://doi.org/10.1142/P850.

Campuzano, S.A., Gómez-Paccard, M., Pavón-Carrasco, F.J., Osete, M. L., 2019. Emergence and evolution of the south atlantic anomaly revealed by the new paleomagnetic reconstruction shawq2k. Earth Planet. Sci. Lett. 512, 17–26. https://doi.org/10.1016/j.epsl.2019.01.050.

Chen, Roeder, J.L., Fennell, J.F., Lyons, L., Lambour, R.L., Schulz, M., 1999. Proton ring current pitch angle distributions: Comparison of simulations with crres observations. J. Geophys. Res.: Space Phys. 104, 17379–17389. https://doi.org/10.1029/1999JA900142Citations.

Chen et al., 1984. Introduction to Plasma Physics and Controlled Fusion, vol. 1. Springer.

Davies, C.J., Constable, C.G., 2020. Rapid geomagnetic changes inferred from earth observations and numerical simulations. Nature Commun. 11, 1–10. https://doi.org/10.1038/s41467-020-16888-0.

Ebihara, Y., Miyoshi, Y., 2011. Dynamic inner magnetosphere: A tutorial and recent advances. In: The Dynamic Magneto. sphere, Springer, pp. 145–187, doi:10.1007/978-94-007-0501-2.

Finlay, C.C., Aubert, J., Gillet, N., 2016a. Gyre-driven decay of the earth's magnetic dipole. Nature Commun. 7, 1–8. https://doi.org/10.1038/ncomms10422.

Finlay, C.C., Olsen, N., Kotsiaros, S., Gillet, N., Tøffner-Clausen, L., 2016b. Recent geomagnetic secular variation from swarm and ground observatories as estimated in the chaos-6 geomagnetic field model. Earth, Planets Space 68, 112. https://doi.org/10.1186/s40623-016-0486-1.

Gillet, N., Jault, D., Finlay, C., Olsen, N., 2013. Stochastic modeling of the earth's magnetic field: Inversion for covariances over the observatory era. Geochem. Geophys. Geosyst. 14, 766–786. https://doi.org/10.1002/ggge.20041.

Girgis, K.M., Hada, T., Matsukiyo, S., 2020. Solar wind parameter and seasonal variation effects on the south atlantic anomaly using tsyganenko models. Earth, Planets Space 72, 1–17. https://doi.org/10.1186/s40623-020-01221-2.

Heirtzler, J.R., 2002. The future of the south atlantic anomaly and implications for radiation damage in space. J. Atmos. Solar Terr. Phys. 64, 1701–1708. https://doi.org/10.1016/S1364-6826(02)00120-7.

Heynderickx, D., 1996. Comparison between methods to compensate for the secular motion of the south atlantic anomaly. Radiation Measur. 26, 369–373.

Liu, L., Olson, P., 2009. Geomagnetic dipole moment collapse by convective mixing in the core. Geophys. Res. Lett. 36. https://doi.org/10.1029/2009GL038130.

Luther, H., 1968. An explicit sixth-order runge-kutta formula. Mathe. Comput. 22, 434–436. https://doi.org/10.1090/S0025-5718-68-99876-1.

Millan, R., Baker, D., 2012. Acceleration of particles to high energies in earth's radiation belts. Space Sci. Rev. 173, 103–131. https://doi.org/10.1007/s11214-012-9941.

Mozer, F., Bale, S., Bonnell, J., Chaston, C., Roth, I., Wygant, J., 2013. Megavolt parallel potentials arising from double-layer streams in the earth's outer radiation belt. Phys. Rev. Lett. 111, 235002. https://doi.org/10.1103/PhysRevLett.111.235002.

Mukherjee, G., Rajaram, R., 1981. Motion of charged particles in the magnetosphere. Astrophys. Space Sci. 74, 287–301. https://doi.org/10.1007/BF00656440.

Navabi, M., Barati, M., 2017. Mathematical modeling and simulation of the earth's magnetic field: A comparative study of the models on the spacecraft attitude control application. Appl. Math. Model. 46, 365–381. https://doi.org/10.1016/j.apm.2017.01.040.

Öztürk, M.K., 2012. Trajectories of charged particles trapped in earth's magnetic field. Am. J. Phys., 80 https://doi.org/10.1119/1.3684537.

Pavon-Carrasco, F.J., De Santis, A., 2016. The south atlantic anomaly: The key for a possible geomagnetic reversal. Front. Earth Sci. 4, 40. https://doi.org/10.3389/feart.2016.00040.

Qin, M., Zhang, X., Ni, B., Song, H., Zou, H., Sun, Y., 2014. Solar cycle variations of trapped proton flux in the inner radiation belt. J. Geophys. Res.: Space Phys. 119, 9658–9669. https://doi.org/10.1002/2014JA020300.

Ripoll, J.F., Claudepierre, S.G., Ukhorskiy, A.Y., Colpitts, C., Li, X., Fennell, J.F., Crabtree, C., 2020. Particle dynamics in the earth's radiation belts: Review of current research and open questions. J. Geophys. Res.: Space Phys. 125. https://doi.org/10.1029/2019JA026735, e2019JA026735.

Rodrigues, R.R., Taschetto, A.S., Gupta, A.S., Foltz, G.R., 2019. Common cause for severe droughts in south america and marine heatwaves in the south atlantic. Nat. Geosci. 12, 620–626. https://doi.org/10.1038/s41561-019-0393-8.

Soni, P.K., Kakad, B., Kakad, A., 2020. Simulation study of motion of charged particles trapped in earth's magnetosphere. Adv. Space Res. https://doi.org/10.1016/j.asr.2020.10.020.

Suttie, N., Holme, R., Hill, M.J., Shaw, J., 2011. Consistent treatment of errors in archaeointensity implies rapid decay of the dipole prior to 1840. Earth Planet. Sci. Lett. 304, 13–21. https://doi.org/10.1016/j.epsl.2011.02.010.

Thébault, E., Finlay, C.C., Beggan, C.D., Alken, P., Aubert, J., Barrois, O., Bertrand, F., Bondar, T., Boness, A., Brocco, L., et al., 2015. International geomagnetic reference field: the 12th generation. Earth, Planets Space 67, 79. https://doi.org/10.1186/s40623-015-0228-9.

Ye, Y., Zou, H., Zong, Q., Chen, H., Wang, Y., Yu, X., Shi, W., 2017. The secular variation of the center of geomagnetic south atlantic anomaly and its effect on the distribution of inner radiation belt particles. Space Weather 15, 1548–1558. https://doi.org/10.1002/2017SW001687.

Zhu, C., Liu, Z., 2020. Weakening atlantic overturning circulation causes south atlantic salinity pile-up. Nature Climate Change, 1–6. https://doi.org/10.1038/s41558-020-0897-7.